Journal of Materials Chemistry B

ROYAL SOCIETY OF CHEMISTRY

PAPER

View Article Online
View Journal | View Issue

Cite this: J. Mater. Chem. B, 2023, 11, 4428

The revelation of glucose adsorption mechanisms on hierarchical metal–organic frameworks using a surface plasmon resonance sensor†

Gilang Gumilar,*[abc] Silvia Chowdhury,[d] Ganes Shukri,[bc] Aep Patah,[e] Nugraha Nugraha,[bc] Joel Henzie,[f] Isa Anshori,[g] Yusuf Valentino Kaneti[d] and Brian Yuliarto *[bc]

The gold layer on the surface plasmon resonance (SPR) sensor chip cannot detect small molecules, such as glucose without the use of specific receptors. Metal–organic frameworks (MOFs) are useful in biosensing technologies for capturing and co-localizing enzymes and receptors with the target biomolecule. In many previous studies, the properties of the MOFs were often ignored, with these studies focusing on the selection of appropriate receptors. To take advantage of the unique properties of MOFs in biosensors, one must also consider the technique and transducer used because these aspects will strongly influence the detection mechanism. In this work, we have investigated for the first time, the applications of hierarchical metal-BDC (M-BDC) MOFs for glucose detection using the SPR technique without the use of specific receptors. The underlying interactions and adsorption mechanisms were analyzed using adsorption isotherm and kinetic models. The sensing measurements show that the SPR chips functionalized with M-BDC MOFs exhibit higher sensitivity and lower limit of detection (LOD). Specifically, the sensitivity follows the order of Zr-BDC > Cu-BDC > Mn-BDC > Ni-BDC > bare Au SPR chips with the LOD in the order of Zr-BDC < Mn-BDC < Ni-BDC < Cu-BDC < bare Au SPR chips. The selectivity test results reveal that Zr-BDC exhibits a decent selectivity to glucose in the presence of other interfering compounds, such as ascorbic acid, uric acid, maltose, and urea. These results demonstrate the promising potential of MOFs for SPR biosensing.

Received 22nd January 2023,
Accepted 12th March 2023

DOI: 10.1039/d3tb00138e

rsc.li/materials-b

1. Introduction

The blood glucose level is one of the most important parameters for monitoring diabetes. Diabetes is commonly caused by the inability of the pancreas to meet the demand for insulin in the body or the ineffective use of insulin by the body. Diabetes mellitus (DM) is divided into two categories, namely, type 1 and type 2. Type 1 diabetes is referred to as insulin-dependent or juvenile/childhood-onset diabetes characterized by a lack of insulin production. Meanwhile, type 2 diabetes, also known as non-insulin-dependent or adult-onset diabetes, is caused by the ineffective use of insulin by the body.[1] A high glucose level in the blood or urine may indicate either that the insulin is not used effectively by the body or the pancreas is unable to produce sufficient insulin for the body. The blood glucose level under physiopathological conditions is controlled by the human body to be around 2–30 mM.[2,3] According to the World Health Organization (WHO), the number of diabetics significantly rose from 108 million adults in 1980 to 422 million adults in 2014. Furthermore, the International Diabetes Federation (IDF) projected that the number of diabetics would increase to 592 million by 2035.[1,4] To minimize the risk of diabetes, it is important to develop an inexpensive sensing technology that can detect and monitor blood glucose levels.

[a] Faculty of Vocational Studies, Institut Teknologi Sains Bandung, Central Cikarang, Bekasi 17530, Indonesia. E-mail: gilang.gumilar@itsb.ac.id
[b] Research Center for Nanoscience and Nanotechnology (RCNN), Institut Teknologi Bandung, Bandung 40132, Indonesia. E-mail: brian@itb.ac.id
[c] Advanced Functional Materials Research Group, Faculty of Industrial Technology, Institut Teknologi Bandung, Bandung 40132, Indonesia
[d] School of Chemical Engineering and Australian Institute for Bioengineering and Nanotechnology (AIBN), The University of Queensland, Brisbane, QLD 4072, Australia
[e] Inorganic & Physical Chemistry Research Division, Institut Teknologi Bandung, Bandung 40132, Indonesia
[f] International Center for Materials Nanoarchitectonics (WPI-MANA), National Institute for Materials Science (NIMS), 1-1 Namiki, Tsukuba, Ibaraki 305-0044, Japan
[g] Lab-on-Chip Group, Biomedical Engineering Department, Institut Teknologi Bandung, Bandung 40132, Indonesia

† Electronic supplementary information (ESI) available. See DOI: https://doi.org/10.1039/d3tb00138e

There has been growing interest in the development of optical sensors for detecting blood glucose levels. Surface plasmon resonance (SPR) sensing is at the forefront of this research because light can excite free electrons on the surface of a noble metal, such as gold (Au) or silver (Ag), to generate surface plasmon polaritons (SPPs). These SPPs propagate as spatially confined evanescent waves in a narrow region on the top surface of the metal and interact with the surrounding dielectric environment.[5–7] Adsorption of the target analyte by the ligand will change the SPP resonance angle (θ_{SP}) further, allowing for the real-time monitoring of molecular binding without the need for labeling. SPR sensors have fast responses, high sensitivity, and relatively high specificity depending on the analyte-capturing ligand.[8–10] However, they are the most sensitive to large molecular weight biomolecules because the large size generates a greater change in the refractive index. Thus, small molecules like glucose ($\sim$180 Da) are difficult to detect using SPR sensors.[8,11]

To overcome this challenge, several studies have employed surface functionalization as a strategy to enhance the adsorption of small molecules. For example, polymers,[12,13] zinc oxide,[9,10] and silica-based glucose-sensitive membranes[14] have all been employed to improve glucose detection with SPR. These studies use glucose oxidase (GO_x) to enhance surface binding of glucose molecules. However, the enzymatic activity of GO_x is highly dependent on pH and temperature and may decrease over time.[3,15,16] Besides, in the immobilization process onto the sensor surface, the use of polymers also requires a strong adhesive compound.[16] Other studies used boronic acid compounds with high affinity towards glucose, but they were highly dependent on the pH.[15,17,18] Glucose/galactose binding proteins (bacteria) have also been used in the detection of glucose by SPR, which led to a good response, even near the minimum concentration of glucose in the human body.[11] Unfortunately, the SPR biosensor required labeling and genetic engineering to detect high concentrations of glucose.[15]

Metal oxides, metal hydroxides, and MOFs have been previously employed in non-enzymatic glucose detection.[19–25] MOFs can increase the bonding interactions with the analyte and serve as active sites to drive electrocatalytic reactions. Host–guest interactions because of Lewis acid or base sites in ligands, open metal sites, hydrophobic interactions, and aromatic groups in MOFs can be utilized to increase the selectivity towards the target analyte. Moreover, the large surface area of MOFs provides rich active sites for catalytic processes and the interconnected porosity eases the diffusion of the analyte to access the active sites. The electron donor–acceptor activity on the MOF structure ligands affects the orbital energy levels of the electrochemical devices.[26–28] MOFs can greatly enhance glucose adhesion in SPR by coordination with the metal ions and multifunctional organic ligands.[29] For example, Hang *et al.* used the SPR technique to detect glucose using core–shell Au@MIL-100(Fe).[30] This study modified the core–shell MOF with 3-aminophenylboronic acid hemisulfate (PBA) which led to high responses toward glucose in the concentration range of 0–40 mM. The study further revealed that the modification of MOF with PBA could enhance the glucose adsorption by increasing the wavelength shift. Another study employed ZIF-8 as a glucose collector in waveguide-based optical fiber biosensors.[31] The biosensors were coated with a GO_x shell to protect them from harsh environments. The wavelength shift had a linear relationship with the glucose concentration in the range of 1–8 mM with a response coefficient of $\sim$0.5 nm mM^{-1}. Although this optical fiber biosensor showed promising results for glucose detection, the ZIF-8 was only used as a matrix for encapsulating the GO_x, so the MOF did not play a central role in glucose detection.

In a previous report, we employed hierarchical M-BDC MOFs for electrochemical non-enzymatic glucose detection. The results showed that the hierarchical sheet-like Ni-BDC had considerable electrocatalytic activity towards glucose with a sensitivity of 635.9 μA mM^{-1} cm^2 in the concentration range of 0.01–0.8 mM and LOD of 6.68 μM (S/N = 3). Other M-BDC MOFs (M = Cu, Mn, and Zr) did not show any electrochemical response towards glucose, thus indicating the limitations of electrochemical detection.[32] Zeng *et al.* studied several MOFs [ZIF-8, MIL-53(Cr), MIL-96(Al), MIL-100(Cr), MIL-100(Fe), MIL-101(Cr), and UiO-66] for the adsorptive separation of a fructose–glucose mixture. They discovered the presence of strong hydrogen bonding interactions between the hydroxyl groups of glucose and fructose with a Zr metal center in UiO-66 (*i.e.* Zr-BDC).[33] To develop M-BDC MOF-based SPR sensors, we will exploit these interactions and explore the possibility of other functional groups that play a role in glucose binding because the different metal types will affect the open metal sites (OMS) and the available functional groups. Additionally, it is also necessary to study the underlying glucose adsorption mechanisms on the surface of M-BDC MOFs and their interactions in the absence of enzymes or other specific bioreceptors. This will enable the main properties that cause the change of the dielectric constant during the detection to be revealed.

In this work, hierarchical sheet-/plate-like M-BDC (M = Cu, Mn, Ni, and Zr) MOFs were synthesized using our previous method and subsequently hybridized with the Au surface on the SPR chip sensor.[32] The SPR measurements for non-enzymatic glucose sensing were carried out using phosphate buffer saline (PBS) at pH 7.4 in the glucose concentration range 0.1–20 mmol L^{-1}. Then, the dynamic responses of the M-BDC MOFs were analyzed by adsorption isotherms and kinetic models to determine the adsorption mechanisms and to obtain the affinity constants. The results reveal that the M-BDC MOF-functionalized SPR sensors can respond to glucose but with different adsorption mechanisms. The functionalization of bare Au SPR chip sensor with M-BDC can enhance glucose adsorption at low concentrations even without using GO_x or other receptors. Among all the fabricated SPR sensors, the Zr-BDC-functionalized sensor shows the highest sensitivity towards glucose as it has the highest specific area and adsorption capacity. Therefore, this MOF can facilitate effective glucose diffusion, enhance accessibility to the active sites, and promote a high adsorption rate. Moreover, it also exhibits relatively good selectivity towards glucose in the presence of other interfering compounds, such as uric acid (UA), ascorbic acid (AA), urea (U), and maltose (M).

2. Experimental section

The detailed chemicals, fabrication procedures for hierarchical M-BDC (M = Cu, Mn, Ni, and Zr), and functionalization of SPR sensor chips with M-BDC MOFs are provided in the ESI.†

2.1. SPR measurements

The SPR measurements were performed using a NanoSPR 6 device with two-channel systems (NanoSPR LLC, US) and the laser was emitted by the GaAs semiconductor laser with a wavelength of 650 nm through a prism for collimating, polarizing, and coupling processes. The SPR sensorgrams were exhibited in the SPR angular changes and time parameters for each glucose concentration (0.1–20 mmol L^{-1}). A syringe pump was used for injecting the glucose solution into the measurement chamber through a flow cell with a flow rate of 25 μL min^{-1}. The measurement procedures were as follows. First, the baseline was taken by measuring the SPR response for the PBS flows on the chamber in 8 minutes. The glucose solution association onto the M-BDC surface was taken for 8 minutes and the dissociation process (using PBS) took 8 minutes as well. The measurements were carried out in series, that is, after the measurement for one glucose concentration was completed, immediately, the next concentration of glucose was flowed into the chamber until all glucose concentrations were tested.

2.2. Adsorption isotherm studies

Adsorption isotherm analysis was carried out to determine the interactions between glucose molecules and M-BDC MOFs during SPR measurements. The obtained parameters from adsorption isotherm models could be used to obtain information on the sorption mechanism, surface properties, and M-BDC affinity towards glucose. The adsorption experiments reported in previous studies typically employ more than one model.[34–38] This is typically done to determine the adsorption mechanisms and the interactions between glucose and the adsorbent more precisely. Several reports have compared the two-parameter and three-parameter adsorption isotherm models to understand the adsorption process and the adsorbate–adsorbent interaction.[34–38]

Sarıkaya *et al.* modified the general adsorption isotherm model by changing the physical quantity of adsorption capacity (q) with the physical quantity of the intensity change (ΔR) directly.[34] In the present work, the adsorption capacity (q) was changed with the physical quantity of angular change ($\Delta\theta$) and the two-parameter adsorption isotherm models used were Langmuir,[35] Freundlich,[35] Jovanovic,[35] Temkin,[38] and Dubinin–Radushkevich.[38] Meanwhile, the three-parameter adsorption isotherm models used were Langmuir–Freundlich (Sips),[35,39] Vieth–Sladek,[35] Brouers–Sotolongo,[35] Redlich–Peterson,[35] and Toth.[35] The non-linear regression analysis was performed using Origin Lab software. The equations of the adsorption isotherm models are shown Table S1 (ESI†). The isotherm parameters that were used to determine the accuracy of the theoretical model on the experimental data were chosen based on the correlation coefficient (R^2) of the non-linear fitting. If the value of R^2 is closer to 1, the model will be used to predict the glucose adsorption mechanism on the M-BDC system used in the experiment. From the selected model, the sensitivity of the M-BDC-functionalized SPR sensor could be obtained from the linear plot of the model and then analyzed using the linear regression method.

2.3. Adsorption kinetic studies

Adsorption kinetic studies were conducted to analyze the adsorption behavior of glucose on different M-BDC MOFs. In this work, we applied the pseudo-first order,[35,36] pseudo-second order,[35,36] Elovich,[36] and Avrami[35,36] adsorption kinetic models on our experimental data. Similar to the adsorption isotherm model, the physical quantity q in the equation of the adsorption kinetic model was modified into the change in angle ($\Delta\theta$) and it was analyzed using the non-linear regression in Origin Lab software. All adsorption kinetic model equations are given in Table S2 (ESI†).

2.4. Selectivity, reusability, and leaching tests

The selectivity test was carried out using the optimum M-BDC-functionalized SPR sensor, for non-enzymatic glucose sensing in the presence of interfering compounds, such as uric acid (UA), ascorbic acid (AA), urea (U), and maltose (M). The concentrations of the interfering compounds were adjusted to the highest concentration limit in healthy human blood, *i.e.*, 0.45 mmol L^{-1} for UA, 0.11 mmol L^{-1} for AA, 5 mmol L^{-1} for U, and 0.1 mmol L^{-1} for M. The concentration of glucose used in the selectivity test was 5 mmol L^{-1}, which was adjusted to the physiopathological conditions of blood glucose level range (2–30 mmol L^{-1}).[2] In addition, the selectivity test was also conducted using the same concentration of molecules with closely related structures as glucose, such as fructose (F) and sucrose (S). The selectivity relationship of the interfering compounds with glucose is expressed by the selectivity coefficient equation,[34] which is shown in the ESI.† The reusability test was carried out using the optimum M-BDC-functionalized SPR sensor towards 5 mmol L^{-1} glucose for 5 consecutive measurements (for the reusability calculation, please see the ESI†). The leaching test was performed to investigate the stability of the M-BDC MOFs on the surface of SPR chip sensors. The waste solutions obtained after the SPR measurements were collected for further analysis by ICP-OES (Inductively Coupled Plasma – Optical Emission Spectrometry) to identify the presence or absence of Cu, Ni, Mn, and Zr metals after adsorption.

2.5. Characterization

The morphology of the M-BDC MOFs was characterized using a scanning electron microscope (SEM, Hitachi SU-8000) operated at 10 kV. The crystal structure and composition of the M-BDC MOFs were checked by X-ray diffraction (XRD, Rigaku RINT 2500X) with Cu-Kα radiation (λ = 0.15406 nm). The Fourier Transform Infrared (FTIR) spectra of the samples before and after the SPR measurements were collected using a Bruker Alpha in the wavenumber range of 500 to 4000 cm^{-1} to investigate the interactions between the functional groups of

glucose and M-BDC MOFs. X-Ray photoelectron spectroscopy (XPS) was used to investigate the elemental compositions and electronic states of the M-BDC MOFs. In order to calibrate the high-resolution XPS peaks concerning the C 1s peak at 285 eV, CasaXPS software was used. ICP-OES (ICP-OES 715-ES, Varian Inc.) was used to identify the metal content in the waste solutions obtained after the SPR measurements.

2.6. Theoretical calculations

First-principles density functional theory (DFT) calculations were performed using Gaussian 09 package code. Generalized Gradient Approximation using the Perdew–Burke–Ernzerhof (GGA-PBE) functional was used to describe the exchange interaction and electronic correlations. We used the 3–21G basis sets for the H, O and C atoms. Furthermore, LANL2DZ was used for the three representative transition metals considered in this study (Zr, Cu and Ni).

2.7. Detection of glucose in human serum

First, a 1 : 100 volume ratio of human serum in PBS was used to prepare the glucose solution in human serum ($V_{\text{human serum}}$: V_{PBS}). The preparation of glucose solutions with concentrations of 0.1–20 mmol L^{-1} was subsequently done using this human serum solution as the solvent. The SPR measurement conditions for glucose sensing in blood serum were similar to those described in Section 2.1, except that human serum solution was utilized as the measurement medium.

3. Results and discussion

3.1. Structural and compositional characterizations of M-BDC MOFs

As shown in Fig. 1, all the prepared M-BDC samples exhibit a hierarchical 3D morphology, which is an assembly of two-dimensional (2D) plate- or sheet-like particles. The hierarchical Cu-BDC sample is arranged by the stacking of numerous plate-like particles (Fig. 1a). In comparison, the Mn-BDC sample exhibits a hierarchical flower-like morphology which is an assembly of nanosheets (Fig. 1b). Furthermore, the Ni-BDC sample displays a hierarchical multilayered structure which is an assembly of sheet-like particles (Fig. 1c). Furthermore, the Zr-BDC sample has a well-defined hierarchical morphology which is composed of plate-like particles of 59 nm in thickness (Fig. 1d).

The formation of the hierarchical 3D M-BDC MOFs under solvothermal conditions at 135 °C for 24 h is caused by the good solvation of metal ions in solution by acetonitrile which allows for the interaction of metal ions with the deprotonated BDC linker. During the synthesis process, PVP serves as a shape-control agent by decreasing the MOF crystal growth and promoting bind metal cations and metal surfaces through the strong interactions $>C{=}O \rightarrow M$ and forming weak hydrogen bonds with organic molecules.[32,40–45]

XRD patterns of the as-synthesized hierarchical M-BDC MOFs are presented in Fig. 2. The XRD pattern of the hierarchical plate-like Cu-BDC sample matches well with the reference pattern for Cu-BDC with the $C2/m$ space group (CCDC no. 687690),[46] with the major peaks at around 10.3°, 12.2°, 17.26°, and 24.86° assigned to (110), (020), (20$\bar{1}$), and (131) planes, respectively (Fig. 2a). The hierarchical sheet-like Mn-BDC product exhibits peaks at around 9.77°, 10.27°, 18.59°, and 20.75° indexed to (11$\bar{1}$), (20$\bar{2}$), (112), and (311) planes of Mn-BDC with the $C2/c$ space group (Fig. 2b). This results matches with the reference pattern for Mn-BDC (CCDC no. 265904) reported by Rosi *et al.*[47] For the hierarchical sheet-like Ni-BDC sample (Fig. 2c), the XRD pattern is in good agreement with the reference pattern for Ni-BDC (CCDC no. 638866) previously reported by Carton and co-workers.[48] The major peaks observed

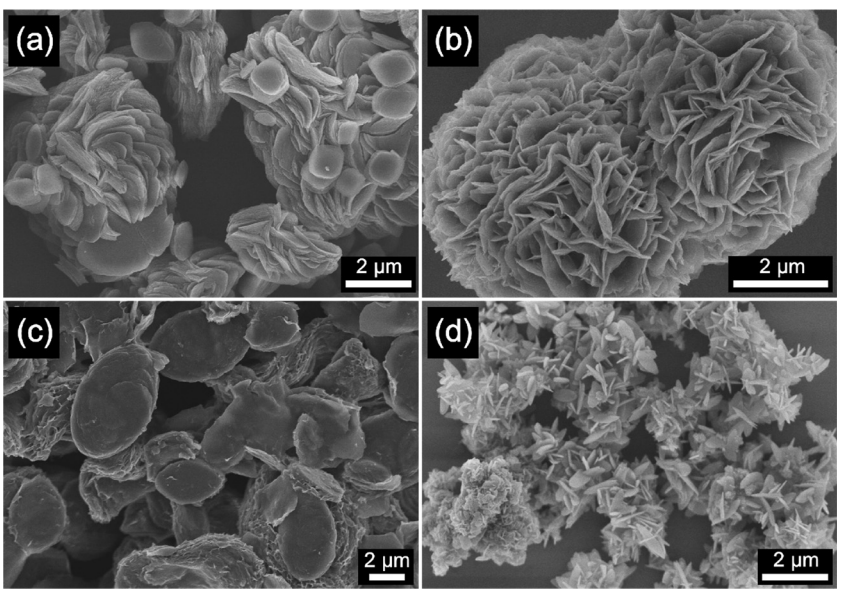

Fig. 1 SEM images of hierarchical (a) Cu-BDC, (b) Mn-BDC, (c) Ni-BDC, and (d) Zr-BDC samples.

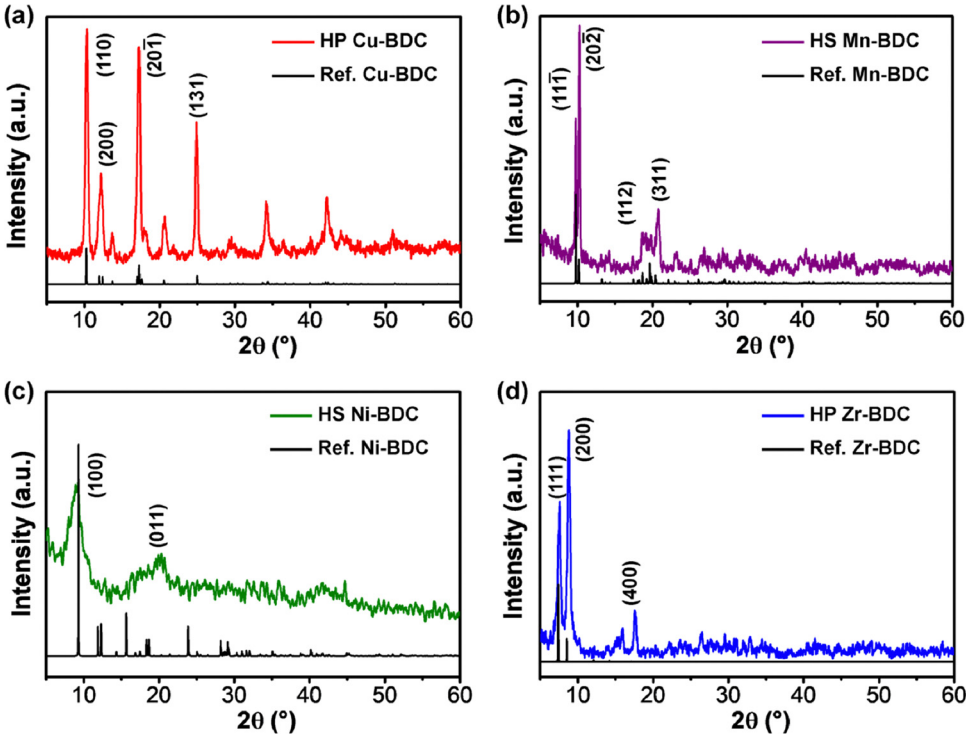

Fig. 2 XRD patterns of hierarchical (a) Cu-BDC, (b) Mn-BDC, (c) Ni-BDC, and (d) Zr-BDC. HS = Hierarchical sheet-like and HP = Hierarchical plate-like.

at around 9.26° and 20.2° can be assigned to the (100) and (400) planes of Ni-BDC with the $P\bar{1}$ space group. As seen in Fig. 2d, the XRD pattern of the hierarchical plate-like Zr-BDC sample displays strong peaks at approximately 9.77°, 10.27°, and 20.75° that can be indexed to the (111), (200), and (400) planes of Zr-BDC with the $Fm\bar{3}m$ space group (CCDC no. 733458).[49,50]

3.2. SPR measurements

3.2.1. Dynamic response. The dynamic responses of the M-BDC-functionalized SPR sensors generally increase with increasing glucose concentration from 0.1 to 20 mmol L^{-1}, as is evident in Fig. 3. The bare Au substrate without M-BDC (Fig. 3a) shows a response starting from 5 mmol L^{-1}. However, the observed responses toward 0.1–2.5 mmol L^{-1} are indistinguishable from the noise. This phenomenon indicates that low glucose concentrations are insufficient to cause a measurable change in the interface of Au layer-glucose refractive index. In contrast, after the deposition of M-BDC MOFs onto the surface of the Au substrates, the response signal can be distinguished from the noise at such low concentrations. This implies that the implementation of M-BDC MOFs can enhance the glucose adsorption of the SPR chip sensor (sensing ability) at low concentrations.

The Cu-BDC-functionalized SPR sensor shows angular changes of 0.0106°, 0.0064°, 0.0072°, 0.0546°, 0.0483°, and 0.0829° upon exposure to 0.1, 1, 2.5, 5, 10, and 20 mmol L^{-1} of glucose (in PBS solution), respectively (Fig. 3b). However, after the ablution process of 0.1 mmol L^{-1} glucose from the chip surface with PBS solution, the SPR signal initially decreases until below the baseline and becomes stabilized after running the PBS for the dissociation process at 1 mmol L^{-1} of glucose. However, beyond this point, the response of the Cu-BDC-based SPR sensor continues to increase with increasing glucose concentration, as normally expected. The initial decrease in the SPR signal of Cu-BDC may be caused by its lower stability in an aqueous environment, leading to some structural decomposition due to the hydrolysis reaction between water molecules and the Cu–O–C group in Cu-BDC.[51–53] Similar to the case of Cu-BDC, the response of the Ni-BDC-based SPR sensor initially also decreases at the beginning between 0.1 and 1 mmol L^{-1} of glucose (Fig. 3c). However, above this concentration, the response continues to increase with the rise in concentration up to 20 mmol L^{-1}. The angular changes towards glucose concentrations of 0.1, 1, 2.5, 5, 10, and 20 mmol L^{-1} are 0.0021°, 0.0006°, 0.0103°, 0.0494°, 0.0511°, and 0.0727°, respectively, for the Ni-BDC-based SPR sensor. Although the SPR signals of both sensors initially decrease at the beginning, the dynamic responses towards glucose are still distinguishable from the baseline for each glucose concentration and an upward trend in response is subsequently observed for both sensors.

Unlike Cu-BDC and Ni-BDC, the response of the Mn-BDC-functionalized SPR sensor appears to increase continuously with the increase of glucose concentration up to 5 mmol L^{-1} of glucose (Fig. 3d). This may have occurred because Mn-BDC is less stable in the aqueous environment. Based on the principle of coordination chemistry, the metal–ligand bond in Mn-BDC is less stable so kinetically, to coordinate in solution, the ligand will tend to compete with solvent molecules, such as water.[54] Consequently, the dynamic response of the Mn-BDC-based SPR sensor continues to increase even without the addition of

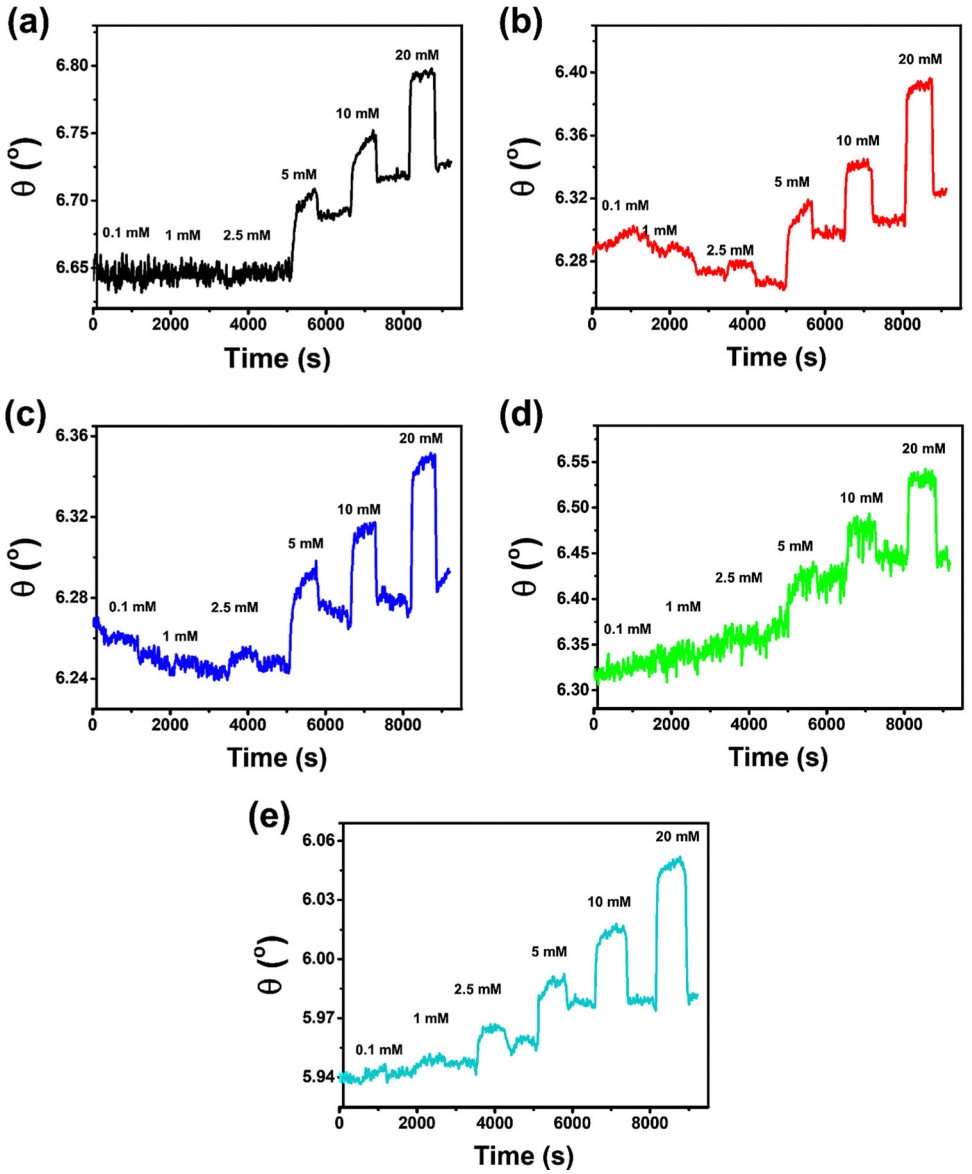

Fig. 3 Dynamic responses of M-BDC-functionalized SPR sensors towards different concentrations of glucose (0.1, 1, 2.5, 5, 10, and 20 mmol L^{-1} in PBS solution): (a) bare Au substrate, (b) Cu-BDC, (c) Ni-BDC, (d) Mn-BDC, and (e) Zr-BDC.

glucose because Mn-BDC may bind directly with the water molecules. The angular changes produced by the interaction between Mn-BDC and glucose at concentrations of 0.1, 1, 2.5, 5, 10, and 20 mmol L^{-1} are 0.0147°, 0.0117°, 0.0203°, 0.0568°, 0.0591°, and 0.0850°, respectively. For the Zr-BDC-functionalized SPR sensor (Fig. 3e), the response that is generated upon exposure to PBS solution at the beginning of measurement appears stable. Then, after 0.1 mmol L^{-1} of glucose solution is injected, the dynamic response is observed to increase and the dissociation process with the use of PBS solutions, response decreased slightly. The angular changes produced by the Zr-BDC-based SPR sensor at glucose concentrations of 0.1, 1, 2.5, 5, 10, and 20 mmol L^{-1} are 0.0006°, 0.0076°, 0.0185°, 0.0431°, 0.1177°, and 0.1496°, respectively. These results clearly indicate that the greater the glucose concentration, the greater the response of the Zr-BDC-functionalized SPR sensor.

The detection of 0.1 mmol L^{-1} glucose by the SPR sensors based on Cu-BDC, Mn-BDC, and Ni-BDC MOFs is somewhat unsatisfactory. At low glucose concentrations (0.1–1 mmol L^{-1}), there may be binding competition between glucose and water molecules in these M-BDC MOFs. Hence, the dynamic responses obtained at such low concentrations may be less reliable. Therefore, the glucose concentration of 0.1 mmol L^{-1} in the case of Cu-BDC, Mn-BDC, and Ni-BDC was not included in the non-linear regression analysis.

3.2.2. Isotherm data analysis. The adsorption isotherm shows the number of molecule distribution between the liquid and solid phases when the adsorption process reaches an equilibrium.[38] The non-linear regression method was used to

obtain the adsorption isotherm parameters. The results show that Cu-BDC, Mn-BDC and Ni-BDC exhibit Langmuir–Freundlich adsorption behavior while Zr-BDC follows the Brouers–Sotolongo adsorption behavior (Fig. 4a) with R^2 for Cu-BDC, Mn-BDC, Ni-BDC and Zr-BDC being 0.8867, 0.93964, 0.99879, and 0.99643, respectively. (The detailed non-linear regression analysis comparison of two- and three-parameter adsorption isotherm models for M-BDC are shown in Fig. S2 (ESI†), whereas the obtained parameters can be seen in Tables S3 and S4 (ESI†) for two- and three-parameters, respectively).

According to the Langmuir–Freundlich adsorption model, the distribution of adsorption energy occurs on a heterogeneous surface where the adsorbate adsorption with high concentration becomes the Langmuir isotherm model and, at low concentration, the adsorption mechanism becomes the Freundlich model.[39] The Freundlich model determines the adsorption process with the adsorbate binding mechanism on a multilayer site whereas the Langmuir model assumes binding at a homogeneous binding site.[34] The heterogeneous parameter (M_{LF}) values for Cu-BDC, Mn-BDC and Ni-BDC are 1.3251,

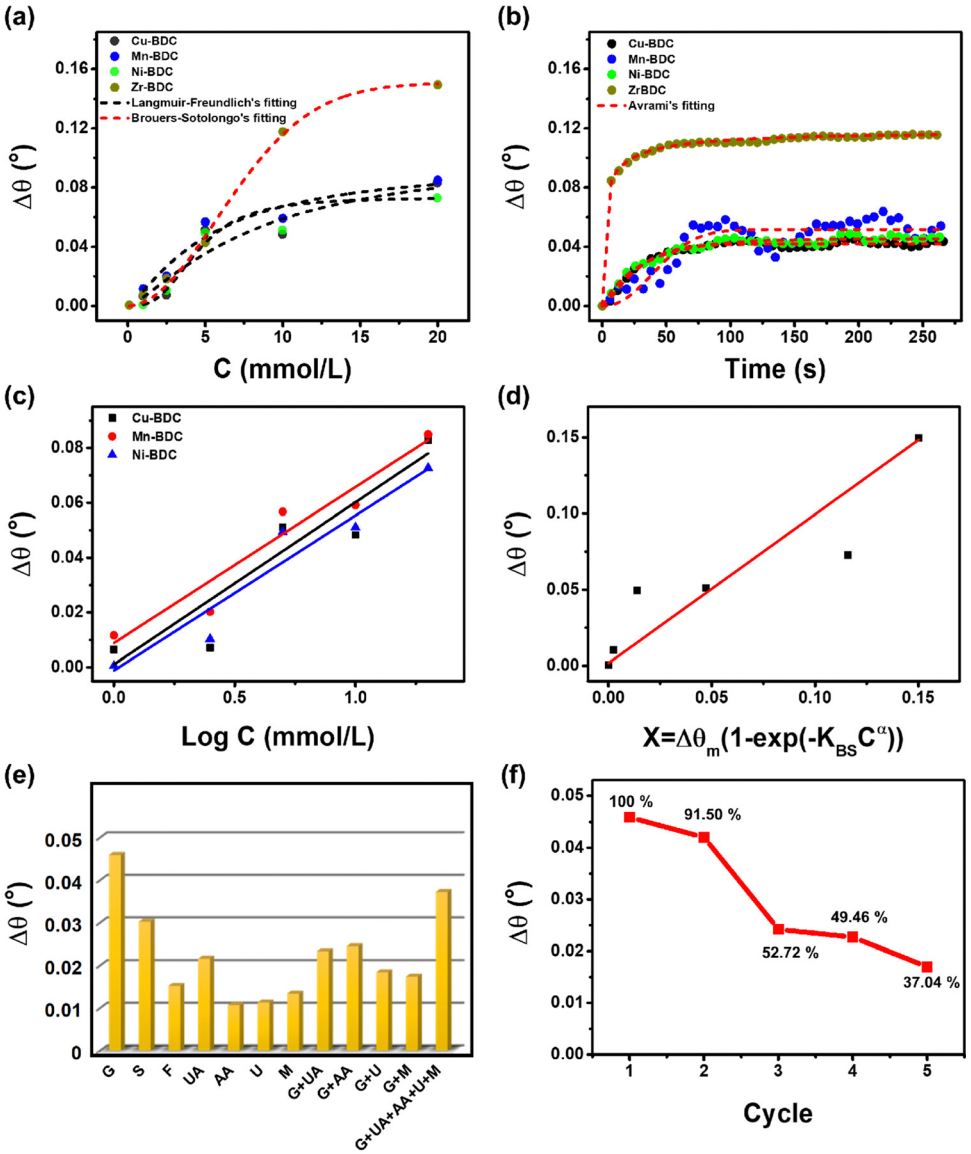

Fig. 4 (a) Non-linear regression curves of Langmuir–Freundlich adsorption isotherm models for glucose-M-BDC (M = Cu, Mn, and Ni) and Brouers–Sotolongo for glucose-Zr-BDC. (b) Non-linear regression curves of the Avrami adsorption kinetic models for glucose-M-BDC (M = Cu, Mn, Ni, and Zr). (c) Calibration curves of the dynamic responses of the M-BDC-functionalized SPR sensors towards glucose: Cu-BDC (black), Mn-BDC (red), and Ni-BDC (blue) are obtained by applying linear fitting to the $\Delta\theta$ *vs.* log C plots (Langmuir–Freundlich model), and (d) Zr-BDC is obtained by applying linear fitting to the $\Delta\theta$ *vs.* $X = \Delta\theta_m [1 - \exp(-K_{BS} C^{\alpha})]$ plots (Brouers–Sotolongo model). (e) Bar diagrams showing the angular changes of the Zr-BDC-functionalized SPR sensor upon exposure to various molecules [5 mM glucose (G), 5 mM sucrose (S), and 5 mM fructose (F), 0.45 mM uric acid (UA), 0.11 mM ascorbic acid (AA), 5 mM urea (U), and 0.1 mM maltose (M)]. (f) The corresponding percentage of the dynamic response of Zr-BDC-functionalized SPR sensor to 5 mmol L^{-1} glucose after the nth measurement compared to the first measurement.

1.28131, and 2.95308, respectively, which are greater than 1. This indicates that in these MOFs, the adsorption process occurs by cooperative interactions as described in the adsorption isotherm model. In cooperative interactions, the adsorbate has the ability to bind at one site on the adsorbent, which in turn, affects other binding sites on the same adsorbent (binding of different species on a homogeneous layer).[55,56] In comparison, the Zr-BDC-based SPR sensor follows the Brouers–Sotolongo adsorption isotherm model where the interaction has a high heterogeneity and is complex in terms of the sorption energy distribution. The high heterogeneity of the Zr-BDC surface in glucose adsorption can be identified from the value of exponent α, where the greater the value, the higher the heterogeneity.[57–59] The obtained exponent α value from the non-linear regression analysis is 1.95791. Since the exponent $\alpha > 1$, the adsorption process is a slow initial biosorption kinetics process so the active sites would have dissimilar energy.[57] Further analyses of the adsorption isotherm data are provided in the ESI.†

The maximum adsorption capacity ($\Delta\theta_m$) values of Cu-BDC, Mn-BDC, Ni-BDC, and Zr-BDC are 0.10432 mmol g^{-1}, 0.09717 mmol g^{-1}, 0.07345 mmol g^{-1}, and 0.15067 mmol g^{-1}, respectively. The $\Delta\theta_m$ value of Zr-BDC is the highest among the samples, due to the higher surface area of this compared to the other M-BDC MOFs. From our previous work, the specific areas of hierarchical Zr-BDC, Mn-BDC, Cu-BDC, and Ni-BDC samples were measured to be 1248.4, 93.7, 90.2, and 34.7 m^2 g^{-1}, respectively.[32] Therefore, the specific surface area plays a major role in increasing the adsorption capacity.[60] The affinity constants for Cu-BDC, Mn-BDC, Ni-BDC and Zr-BDC are 0.12146, 0.18805, 0.22405, and 0.01614 mmol L^{-1}, respectively.

3.2.3. Kinetic data analysis. The kinetic adsorption analysis was carried out to understand the dynamics of glucose–M-BDC interaction which was expressed by the adsorption rate constant. The glucose concentration used for the kinetic analysis was 10 mmol L^{-1} for 4 minutes. In this case, a time of 4 minutes was chosen because of consideration with respect to the point-of-care device in health facilities. The non-linear regression curve for each model is shown in Fig. S3 (ESI†) and the acquired adsorption parameters and the R^2 values of the kinetic model fitting are provided in Table S5 (ESI†).

From the non-linear regression results (Table S5, ESI†), it can be concluded that, for all M-BDC MOFs, the highest correlation coefficient is obtained using the Avrami model with R^2 values of 0.96849, 0.78500, 0.95603, and 0.98447 for Cu-BDC, Mn-BDC, Ni-BDC, and Zr-BDC, respectively (Fig. 4b). The adsorption processes that take place can be identified by the values of K_{AV} and n_{AV}. In the study of Li *et al.*, n_{AV} was found to be closely related to the process of releasing adsorbates from the adsorbents;[29] however, in this study, n_{AV} is associated with the glucose adsorption by M-BDC. If the n_{AV} value is in the range of 0.3–1, the adsorption process that occurs is a diffusion process, while n_{AV} values between 1 and 2 indicate that the adsorption process is similar to a first-order kinetic process.[29] However, according to the report of Oladoja *et al.*,[61] if the n_{AV} value is between 1 and 2, it indicates a one-dimensional (1D) crystal growth. Both studies used the same parameters to describe the different functions, *i.e.*, adsorption and crystal growth. Therefore, Oladoja *et al.*[61] stated that 2D crystal growth occurs when the n_{AV} value is in the range of 2–3 and using a similar analogy, the adsorption mechanism is a second-order kinetic process.

The Cu-BDC MOF has an n_{AV} value of 1.28621, hence, the adsorption process is a first-order kinetic process. In contrast, the adsorption of glucose on the surface of Ni-BDC and Zr-BDC occurs through diffusion, as indicated by their n_{AV} values of 0.92541 and 0.3307, respectively. However, for Mn-BDC the value is greater than 2 (2.198); therefore, the adsorption process is a second-order kinetic process. The reaction rate constants (K_{AV}) of all M-BDC MOFs are different with the order being Zr-BDC (0.66681 s^{-1}) > Ni-BDC (0.03987 s^{-1}) > Cu-BDC (0.01291 s^{-1}) > Mn-BDC (1.712×10^{-4} s^{-1}). Based on Avrami's kinetic adsorption parameters, the relationship between K_{AV} and n_{AV} tends to be inversely related, that is, the greater the value of n_{AV}, the smaller the value of K_{AV}. Hence, it can be assumed that the adsorption mechanism determines the adsorption rate constant, K_{AV}. Furthermore, the adsorption of glucose by Zr-BDC occurs by diffusion, so the process is faster compared to first-order (Cu-BDC) and second-order (Mn-BDC) kinetic processes. The second-order kinetic process on Mn-BDC is slower than the glucose adsorption by other M-BDC MOFs because it has the smallest adsorption rate of 1.712×10^{-4} s^{-1}.

3.2.4. Calibration curves for M-BDC non-enzymatic glucose sensing. To determine the LOD, linear fitting was applied to the $\Delta\theta$ *vs.* $\log C$ plot from the Langmuir–Freundlich model (for Cu-BDC, Mn-BDC, and Ni-BDC) and the $\Delta\theta$ *vs.* $X = \Delta\theta_m [1 - \exp(-K_{BS}C^{\alpha})]$ plot from the Brouers–Sotolongo model (for Zr-BDC).[36,62] However, for the bare Au substrate, as the dynamic response only becomes measurable from an initial concentration of 5 to 20 mmol L^{-1}, it does not follow a specific adsorption model (Fig. S4, ESI†). The calibration curves derived from the dynamic responses of M-BDC-functionalized SPR sensors (M = Cu, Mn, and Ni) towards glucose are given in Fig. 4c, whereas the calibration curve for Zr-BDC is given in Fig. 4d, and the obtained parameters are shown in Table 1.

The linear regression analysis of Zr-BDC shows that it has a higher sensitivity (0.99702) than other M-BDC MOFs. Therefore, the order of sensitivity from the highest to the lowest is Zr-BDC > Cu-BDC > Mn-BDC > Ni-BDC > bare Au substrate. In terms of LOD, Zr-BDC shows the best LOD followed by Mn-BDC, Ni-BDC, Cu-BDC, and bare Au substrate, respectively. The use of hierarchical M-BDC as an active layer on the bare Au substrate can enhance the glucose adsorption capacity and therefore, the LODs of the M-BDC functionalized sensors are much lower than that of the bare Au substrate, allowing them to detect lower concentrations of glucose. Other than that, these results indicate that the Zr-BDC-functionalized SPR sensor is superior to those functionalized with Cu-BDC, Mn-BDC, and Ni-BDC in terms of both sensitivity and LOD. Therefore, for selectivity and reusability experiments, the hierarchical plate-like Zr-BDC was used as it is the optimum sample.

Table 1 The parameters obtained from calibration curves

MOFs	Linear equation	Sensitivity	LOD (mmol L^{-1}) (S/N = 3)	Concentration range (mmol L^{-1})	R^2
Bare Au	$\Delta\theta = 0.00151C + 0.04655$	0.00151	14.763	5–20	0.9560
Cu-BDC	$\Delta\theta = 0.05914 \log C + 0.00107$	0.05914	10.383	1–20	0.91254
Mn-BDC	$\Delta\theta = 0.05689 \log C + 0.00887$	0.05689	4.790	1–20	0.95886
Ni-BDC	$\Delta\theta = 0.05653 \log C + 0.00118$	0.05653	4.945	1–20	0.94295
Zr-BDC	$\Delta\theta = 0.97702X + 0.00172$	0.97702	4.499	0.1–20	0.98918

3.2.5. Selectivity. The selectivity test was conducted in the presence of other molecules present in human blood to determine the selectivity of the Zr-BDC-functionalized SPR sensor towards glucose. The selectivity test results show that this sensor shows a considerably higher response to glucose relative to other competing molecules, as seen in Fig. 4e (the corresponding SPR dynamic responses are given in Fig. S5, ESI†). The SPR responses (reflected by angular changes) and the selectivity coefficients of Zr-BDC from the selectivity test results are summarized in Table 2.

In addition, selectivity tests were also carried out on molecules with similar structures to glucose (G), namely sucrose (S) and fructose (F) with the same concentration as glucose. As depicted in Fig. S5a (ESI†), the response curves of the Zr-BDC-based SPR sensor returns to the baseline position following the dissociation of fructose and sucrose; however this is not the case for glucose. This suggests the ability of Zr-BDC to bind G more strongly than S and F. In addition, the angular change upon G exposure is more significant than those to both S and F with the order being G > S > F and k F > k S (see Table 2). Moreover, the characteristics of the three curves are different. For S and F exposure, after the initial increase in the angular change to a certain extent, the response eventually becomes saturated. However, for G exposure, the angular change continues to increase until the dissociation process begins. This phenomenon indicates that glucose continues to be bound by the hydroxyl group in Zr-BDC and saturation has not yet occurred. Hence, it can be deduced that the Zr-BDC is more specific for binding G than S and F.

The angular changes of Zr-BDC towards each interfering compound, in descending order, are G ($\Delta\theta$ = 0.0459°) > UA ($\Delta\theta$ = 0.0216°) > M ($\Delta\theta$ = 0.0459°) > U ($\Delta\theta$ = 0.0113°) > AA ($\Delta\theta$ = 0.0107°) with the selectivity coefficient values being k (UA) = 2.125, k (M) = 3.425, k (U) = 4.062, and k (AA) = 0.0107. The selectivity coefficient value indicates the selectivity of Zr-BDC towards glucose against competing molecules. If it has a value of k = 1, then the selectivity is relatively similar, and if the value of k <1, then Zr-BDC is more selective against competing molecules. As shown in Table 2, the competing molecules have k values >1, so Zr-BDC is not selective towards these compounds, and the response towards glucose can still be distinguished from the others.

Table 2 The angular changes of Zr-BDC in response to glucose and glucose with other interfering compounds and the corresponding selectivity coefficients

Biomolecules	$\Delta\theta$ (°)	K	Biomolecules	$\Delta\theta$ (°)	k
G	0.0459	—	M	0.0134	3.425
S	0.0302	1.518	G + UA	0.0233	1.970
F	0.0152	3.016	G + AA	0.0245	1.873
UA	0.0216	2.125	G + U	0.0184	2.495
AA	0.0107	4.290	G + M	0.0174	2.638
U	0.0113	4.062	G + UA + AA + U + M	0.0372	1.234

$\Delta\theta$ is the angular change.k is the selectivity coefficient.

To ensure the response to glucose can be distinguished from other compounds, selectivity tests were carried out on glucose mixtures with various interfering compounds with the same concentration as glucose. Following the addition of 5 mmol L^{-1} glucose, the response of Zr-BDC to competing molecules was increased, but the angular changes are still lower than that towards glucose itself (Table 2). The angular changes and the selectivity coefficients towards binary mixtures of G + UA, G + AA, G + U, G + M, and G + UA + AA + U + M are 0.0233° (k = 1.970), 0.0245° (k = 1.873), 0.0184° (k = 2.495), 0.0174° (k = 2.638), and 0.0372° (k =1.234), respectively (Fig. S5b, ESI†). These results reveal that Zr-BDC is more likely to interact with glucose even in the presence of other interfering compounds.

3.2.6. Reusability. The reusability test was carried out using a glucose concentration of 5 mmol L^{-1} for five repetitions with the Zr-BDC-functionalized SPR sensor. From Fig. 4f, it is clear that the dynamic response of this sensor gradually decreases from 100% in the 1st measurement to 91.50% in the 2nd measurement to 52.72% in the 3rd measurement to 49.46% in the 4th measurement, and finally to 37.04% in the 5th measurement. After 5 repetitions, the dynamic response is reduced by 62.96%, as seen in Fig. S6, ESI†). The considerable decrease in sensing response may be caused by the strong bonding of the hydroxyl group on glucose with the Zr metal center in Zr-BDC. Hence, some glucose molecules may still remain on the active sites (*i.e.*, not effectively desorbed). The decrease in the response percentage in the second measurement is only 8.50%. This value is still relatively close to the first measurement, so the Zr-BDC-modified SPR sensor can only be used for two consecutive measurements at present. Therefore, the reusability of this sensor may need to be improved further in the future.

3.2.7. Post-adsorption analysis. The analysis of glucose adsorption using adsorption isotherm and kinetic models shows that the four M-BDC samples have different mechanisms. To further investigate the glucose adsorption mechanisms of M-BDC MOFs and their interactions with each other, the M-BDC-functionalized SPR sensors before and after the glucose sensing test were characterized by both FTIR and XPS. The FTIR results

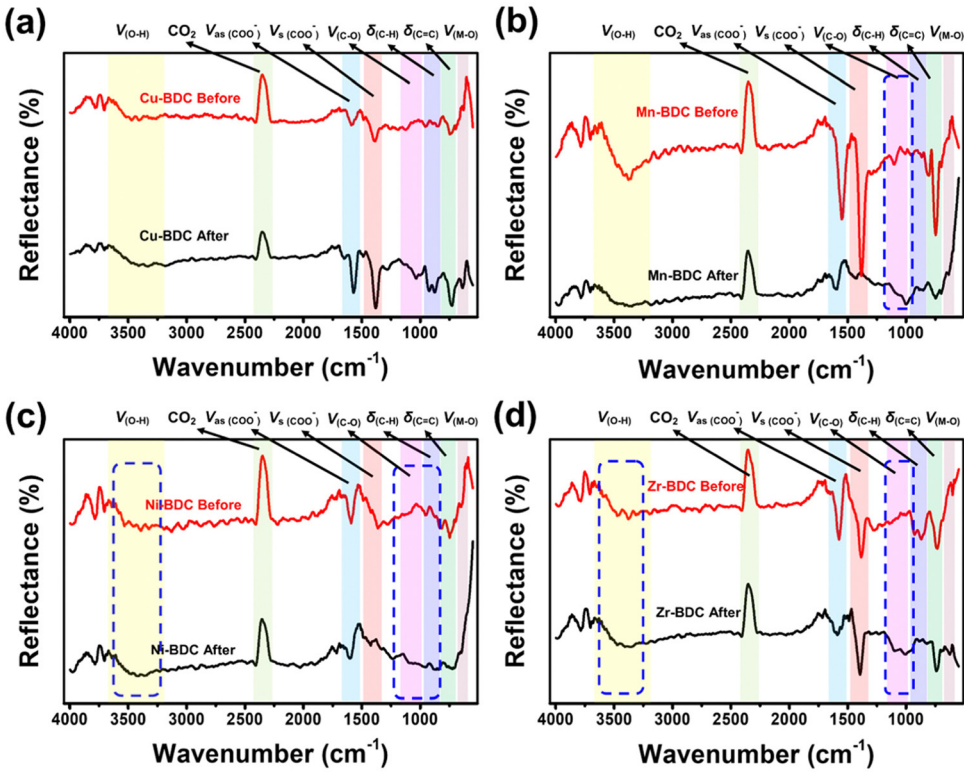

Fig. 5 FTIR spectra of M-BDC-functionalized SPR sensors before and after non-enzymatic glucose sensing: (a) Cu-BDC, (b) Mn-BDC, (c) Ni-BDC, and (d) Zr-BDC.

show that all samples have a negative peak at 2353 cm^{-1}, which may originate from atmospheric CO_2 (Fig. 5). The adsorption of glucose on Cu-BDC changes several functional groups, as shown in Fig. 5a. The intensity of the O–H stretching vibration at ~3404 cm^{-1} increases slightly after the adsorption process. Moreover, the IR bands in the ranges of 1527–1623 cm^{-1} and 1306–1476 cm^{-1} corresponding to asymmetric and symmetric stretching vibrations of the carboxyl groups, respectively, also become much more intense. Similarly, the IR band between 1000 and 1143 cm^{-1} indexed to the C–O stretching vibration along with the C–H and C=C bending vibrations located between 806 and 959 cm^{-1} and 655–800 cm^{-1}, respectively, and the bending vibration of Cu–O at 599 cm^{-1} also become more intense after glucose adsorption. Based on the adsorption analysis, the glucose adsorption on Cu-BDC involves cooperative interactions with the first-order kinetic process. The strengthening of the IR spectra indicates that glucose molecules interact cooperatively with these functional groups. Besides, the lack of broadening of these peaks, may indicate the occurrence of physisorption, where the binding process between the adsorbent and the adsorbate involve electrostatic interactions, van der Waals forces, diffusion, or hydrogen bonding.[63,64]

The IR spectra of Mn-BDC before and after glucose adsorption (Fig. 5b) reveal the weakening of the O–H stretching vibration, the asymmetric and symmetric stretching vibrations of carboxyl group, the C–C and C=O bending vibrations, and Mn–O vibration observed in the original Mn-BDC. However, the C–O stretching vibration at ~1000 cm^{-1} is slightly strengthened. The weakening of the IR bands after the glucose adsorption suggests the occurrence of chemisorption where the functional groups chemically react with the adsorbate and/or competing molecules to form chemical bonds.[63,65] Zhang and co-workers showed that Mn-BDC could react with water molecules through Mn-carboxyl oxygen and Mn-hydroxyl oxygen bonds, accompanied by weakening of the Mn–O bond.[66] The cooperative interaction and second-order kinetic process for glucose adsorption on Mn-BDC may be caused by the simultaneous binding of glucose and water molecules on the active sites, because the molecules used in the adsorption model are assumed to be homogeneous.

In Ni-BDC, several bands are weakened in intensity after the glucose adsorption, namely the asymmetric and symmetrical stretching vibrations of carboxyl groups and the bending vibrations of C=C and Ni–O bonds (Fig. 5c). In contrast, strengthening of the O–H and C–O stretching vibrations and C–H bending vibration (located between 857 and 1147 cm^{-1}) is observed for Ni-BDC after glucose adsorption. This may be attributed to the binding of glucose to Ni-BDC *via* hydroxyl groups at its terminal and hydroxyl bridges. The rearranged hydrogen bonds during the interaction with Ni-BDC can increase the C–H bending vibration and the C–O stretching vibration.

The C–O stretching vibration of Cu-BDC, Mn-BDC, and Ni-BDC at around 1000 cm^{-1} is increased after the glucose adsorption. This increase is due to the effect of M–OH group coordination and the rearrangement of the glucose hydrogen

bond network on metal complexation.[67] The weakening of the M═O bonds in the IR spectra of Cu-BDC, Mn-BDC, and Ni-BDC indicates the release of electrons from the metal center so that the H^+ ion of water donates electrons to O, leading to the formation of the M–OH bond. This process can also increase the stretching vibration of O–H. Unfortunately, the strong polarity of the water molecule through the H and OH groups attached to the M–O bond can also affect the breaking of the metal center-ligand bond so that the degradation or hydrolysis of the M-BDC can occur.[68,69] Still, the hydrolysis reaction between water molecules and M-BDC may lead to the breakage of the metal–ligand bond to form the hydroxide anion-metal bond and proton-displaced ligand bond from the water dissociation process. The hydrolysis of water molecules with M-BDC is expressed as follows.[70,71]

$$M^{n+} - L^{n-} + H_2O \rightarrow M^{n+} - (OH)^- + HL^{(n-1)-} \quad (4)$$

The above explanation shows that cooperative interactions are possible. The competitive reaction that takes place between water and glucose molecules with M-BDC, in the adsorption model, is assumed to be the reaction between the adsorbate and the adsorbent.

For Zr-BDC, the glucose adsorption occurs through biosorption and diffusion. Most of the biosorption process is strongly influenced by the isoelectric charge of the adsorbent surface, which causes the surface to have a neutral charge.[72] The IR bands between 3272 and 3453 cm^{-1}, 946 and 1128 cm^{-1}, and the IR band at 596 cm^{-1}, belonging to the O–H stretching vibration, C–O stretching vibration, and Zr–O, respectively, become more intense after glucose adsorption (Fig. 5d). The increase in the intensities of the O–H and C–O stretching vibrations may be caused by the binding of glucose to Zr-BDC through the hydroxyl group with the terminal and hydroxyl bridges at the Zr6 node of Zr-BDC *via* hydrogen bonding.[33] Moreover, the increase of the Zr═O peak may originate from the binding of the C–O group of glucose with the Zr metal center, which provides the active sites due to material defects originating from the release of the BDC linker. However, there is a possible influence of water molecules on the asymmetric stretching vibration of the carboxyl group, as indicated by the weakening of the IR bands between 1523 and 1629 cm^{-1}, and this phenomenon has been previously explained by DeCoste *et al.*[73] The water molecule interpolates a metal–ligand bond of the framework and replaces the ligand to form a hydrated cation, releasing a free ligand. The reaction is expressed by the equation below.[70,71]

$$M^{n+} - L^{n-} + H_2O \rightarrow M^{n+} - (OH_2)\cdots L^{n-} \quad (5)$$

The above process does not affect the stability of Zr-BDC as it has 12-connected metal clusters so that it is blessed with a tremendous steric-hindrance effect around the metal center. The release of carboxyl bonds provides material defects that are useful for increasing the adsorption capacity.[33,69] Meanwhile, the reduction in C–H peaks after glucose adsorption may be caused by rearrangement of the hydrogen bonds in glucose with Zr-BDC to achieve a saturated and/or neutral surface charge. However, the symmetric stretching vibration of the carboxyl group (1345–1438 cm^{-1}) and the C═C bending vibration (706–798 cm^{-1}) remain relatively unchanged after glucose adsorption.

XPS measurements were conducted to obtain more information about the chemical composition and chemical state of the M-BDC MOFs before and after glucose adsorption, as presented in Fig. 6a–d. The XPS survey spectra presented in Fig. 6a(i–iv) show four peaks at around 285.0, 531.5, 330, 642.5, 856.4, and 935.5 eV, which suggests the presence of C 1s, O 1s, Zr 2p, Mn 2p, Ni 2p, and Cu 2p, respectively.[74,75] To understand the XPS results in detail, all these peaks have been deconvoluted to identify the chemical bonds (Fig. 6b–d). The high-resolution C 1s XPS spectra of Zr-BDC, Mn-BDC, Ni-BDC, and Cu-BDC in Fig. 6b(i–iv) show a C–C/C═C peak at 285.00 eV and carbonyl carbon (C–O) at 285.92, 285.94, 285.94 and 286.05 respectively, carboxylate carbon (O–C═O) corresponds to 287.78, 288.36, 288.75 and 288.56 respectively.[76] The atomic percentages of these bonds are given in Fig. S7a (ESI†). The high-resolution O 1s XPS spectra of Zr BDC, Mn BDC, Ni BDC, and (iv) Cu-BDC can be fitted with three peaks belonging to C–O, C═O and O–H species (Fig. 6c) with the corresponding atomic percentages presented in Fig. S7b (ESI†).

The deconvoluted Zr 2p spectrum of Zr-BDC reveals two major peaks at 182.71 and 185.10 eV with two strong satellite peaks at 183.10 and 185.41 eV (Fig. 6d(i)), which are indicative of Zr^{2+}. The deconvoluted Mn 2p spectrum of Mn-BDC shows the presence of peaks at 641.36 and 652.93 eV with two strong satellite peaks at 643.46 and 653.87 eV (Fig. 6d(ii)), which indicates the presence of Mn^{2+}. Additionally, the characteristic peaks of Mn^{3+} species are also observed at 642.35 and 653.86 eV with the corresponding satellite peaks located at 643.46 eV and 661.46 eV. The deconvoluted Ni 2p spectrum of Ni-BDC reveals the presence of peaks at 856.09 and 873.85 eV with two strong satellite peaks at 860.68 and 876.77 eV (Fig. 6d(iii)), which are indicative of Ni^{2+}. Additionally, the characteristic peaks of Ni^{3+} species are observed at binding energies of 857.12 and 874.93 eV with two satellite peaks at 863.95 eV and 880.81 eV. The deconvoluted Cu 2p spectrum of Cu-BDC reveals the existence of peaks at 934.68 and 954.60 eV with two strong satellite peaks at 940.15 and 960.75 eV (Fig. 6d(iv)), corresponding to Cu^{2+}. Additionally, the characteristic peaks of Cu^{3+} species are observed at binding energies of 935.15 and 955.72 eV with two satellite peaks located at 944.26 eV and 963.55 eV.

After glucose adsorption, the chemical composition and chemical state of the M-BDC MOFs were also analyzed by XPS, as presented in Fig. 6e–h. The XPS survey spectrum of the M-BDC MOFs (M = Zr, Mn, Ni, Cu) presented in Fig. 6e(i–iv) displays peaks at ~285, 531.5, 333.19, 856.36, and 935.18 eV, belonging to C 1s, O 1s, Zr 2p, Mn 2p, Ni 2p, and Cu 2p peaks, respectively.[74,75] After glucose adsorption, the Mn 2p peaks in the Mn-BDC sample disappear, indicating the unstable nature of this MOF in water, unlike Zr-BDC, Ni-BDC, and Cu-BDC.

As seen from Fig. S7 (ESI†), the overall atomic percentage of carbon increases after glucose adsorption for all M-BDC MOFs. This may be due the additional absorption of carbon from

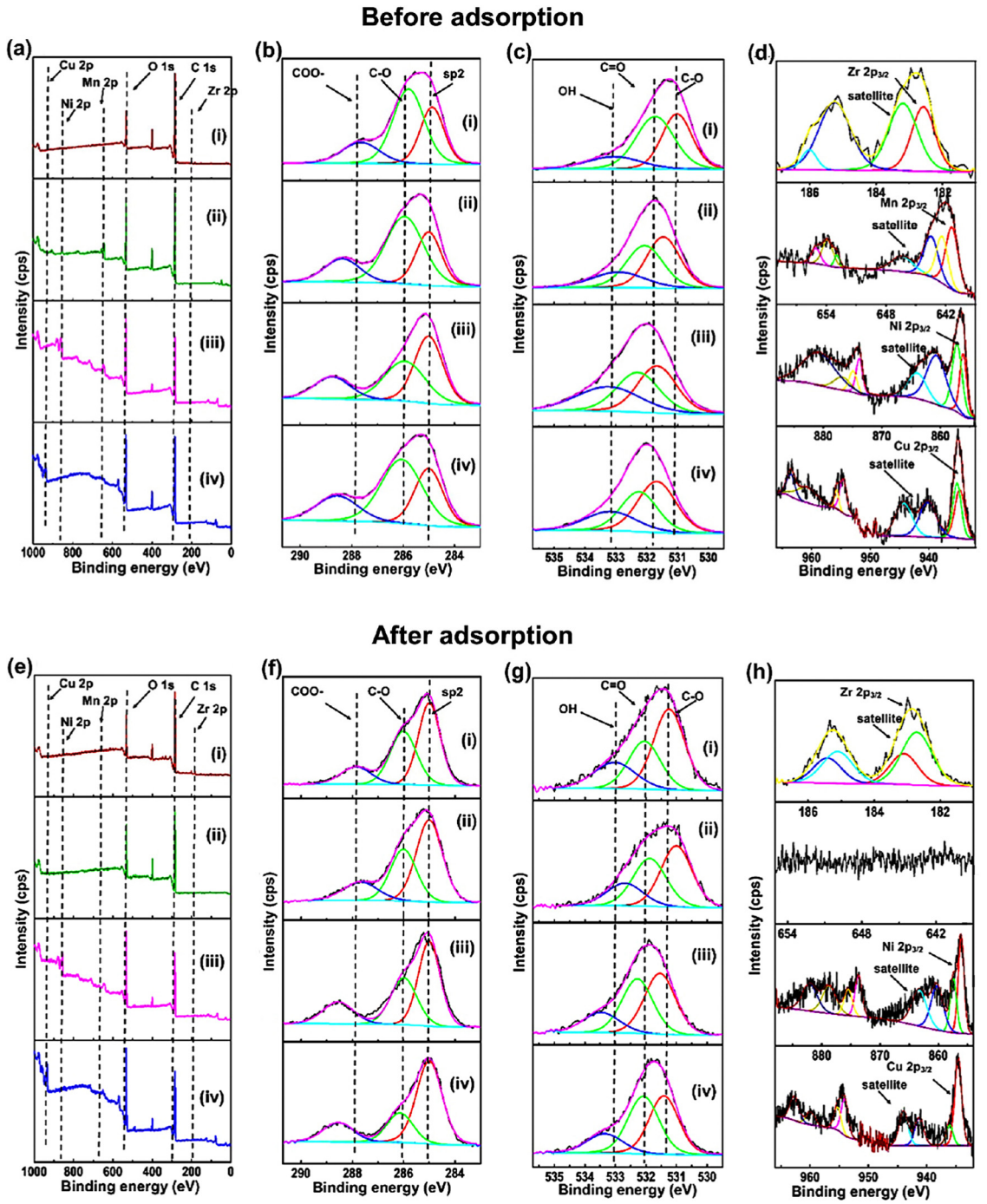

Fig. 6 XPS analysis of (i) Zr-BDC, (ii) Mn-BDC (iii) Ni-BDC and (iv) Cu-BDC before and after glucose adsorption: (a and e) survey spectra; high-resolution XPS spectra for (b and f) C 1s, (c and g) O 1s, and (d and h) M 2p (where M = Zr, Mn, Ni, and Cu).

glucose by the M-BDC MOFs. Hence, the glucose adsorption mechanism involves the removal of carbon from glucose molecules. Compared to Mn-BDC, Ni-BDC, and Cu-BDC, the increase in the atomic percentage of carbon (C–Cis more pronounced in Zr-BDC, which explains for the superior glucose adsorption by Zr-BDC (Fig. S7, ESI†). In contrast, the atomic percentages of carbonyl carbon (C–O) and carboxylate carbon (O–C═O) are decreased for all M-BDC MOFs. The possible glucose adsorption mechanism by M-BDC MOFs is illustrated in Fig. 7.

3.2.8. Possible glucose sensing mechanism of hierarchical M-BDC MOFs. The glucose binding occurs through the O–H and C–O groups on M-BDC MOFs. The evanescence wave provides an electric field to the glucose-M-BDC interface system, and it can polarize the dipole or moves the trapped charge carriers in the interface so the medium relative permittivity and

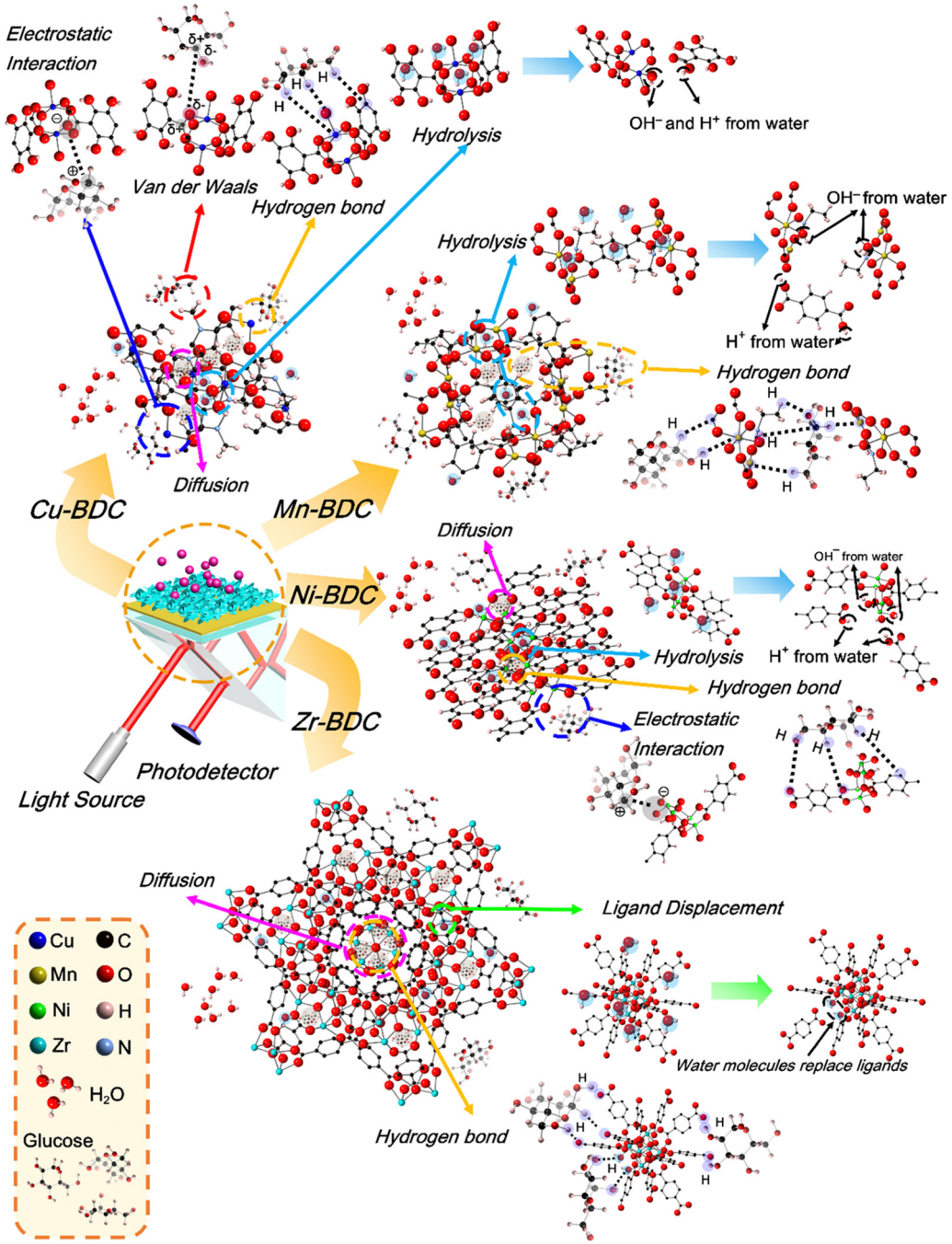

Fig. 7 Schematic illustration of the possible glucose adsorption mechanisms by hierarchical M-BDC MOFs during the SPR sensing process.

the dielectric constant change. This phenomenon increases the system refractive index and affects the laser reflection angle.

The refractive index of the standard or bare SPR sensor chip is 1.61, while for the Zr-BDC thin film prepared by spin coating it is 1.208 and the refractive index of Cu-BDC is 1.34.[77,78] Unfortunately, the refractive index values for Mn-BDC and Ni-BDC have not been reported so far. However, the magnitude of the refractive index is strongly influenced by the pore width of the material; the larger the pore width, the smaller the refractive index.[78] When viewed using Zr-BDC and Cu-BDC data, the sensitivity of Zr-BDC to glucose is higher than that of Cu-BDC despite the smaller refractive index. Therefore, it can be concluded that the refractive index value of M-BDC does not really affect the sensitivity. The main characteristic that affects the changes in the refractive index and the angular change is the porosity of M-BDC MOFs, which can adsorb as much glucose as possible so that its relative permittivity increases.[79,80] However, this still needs to be studied further.

3.2.9. Stability. To further investigate the stability of M-BDC MOFs for SPR biosensing, leaching tests were carried

out on the waste solutions obtained after the glucose sensing measurements to detect any leaching of metal ions from the M-BDC MOF adsorbents. If a metal ion is detected by ICP-OES in the waste solution, it indicates that the M-BDC MOF sample is less stable. From Fig. S8 (ESI†), it can be seen that the concentration of Cu in the waste solution collected after the glucose sensing measurement is below 0.005 mg L^{-1}, thereby indicating that the decomposition of Cu-BDC does not occur. The waste after glucose measurements by Mn-BDC shows the presence of dissolved Mn metal ions with a total concentration of 0.013 mg L^{-1}. For Ni-BDC, the concentration of Ni in the waste solution is 0.011 mg L^{-1}. The presence of Mn and Ni metal ions in the waste solutions indicates that Mn-BDC and Ni-BDC are less stable. Unfortunately, the waste solution for Zr-BDC cannot be characterized by ICP-OES because of the lack of a standard solution for analyzing the Zr metal in our ICP facility.

To further quantify the thermodynamic stability of each M-BDC MOF, we also calculated the decomposition reaction enthalpy of M-BDC (M = Zr, Ni, Cu) in the presence of water molecules using first-principles density functional theory (DFT) calculations (Fig. S9, ESI†). We considered two decomposition reaction models following eqn of (4) and (5). Here, reaction (4) represents a model where the H_2O dissociates into OH^- and H^+ which subsequently attach to the metal ligand and to the oxygen of the dissociated part of the ligand. Meanwhile, reaction (5) represents a model where H_2O is molecularly attached to the metal ligand (without any dissociation). For the two considered reaction models, we found that all dissociation reactions of M-BDC are endothermic, indicating that the degradation of M-BDC is not a spontaneous process. However, further examination of the calculated enthalpies shows that Cu-BDC and Zr-BDC indeed have better thermodynamic stability as compared to Ni-BDC for both reaction models (as shown by the overall higher dissociation enthalpy). These data support the slight degradation of Mn-BDC and Ni-BDC by water molecules, as described earlier in the mechanism section. For future development, it is necessary to modify the M-BDC MOF to increase its water stability.

Following glucose detection, the M-BDC MOF samples were examined using XRD to assess the compositional stability. As shown in Fig. S10 (ESI†), the peak positions of Zr-BDC remain the same after the glucose sensing process; however the intensity of the peaks slightly decreases. In comparison, the peaks of Cu-BDC are shifted after glucose sensing, which may be attributed to a change in lattice parameters (Fig. S10a, ESI†). On Mn-BDC, there is only one peak remaining after glucose sensing while other peaks have either shifted or disappeared (Fig. S10b, ESI†). Meanwhile, Ni-BDC becomes amorphous after the glucose sensing test (Fig. S10c, ESI†). The M-BDC MOF samples that experience changes in lattice parameters or become amorphous after the glucose sensing process are likely to have undergone a phase transformation.[81] These results clearly demonstrate the superior stability of Zr-BDC compared to Cu-BDC, Mn-BDC, and Ni-BDC.

3.2.10. Glucose detection in human serum. To demonstrate the practicality, we further investigated the glucose

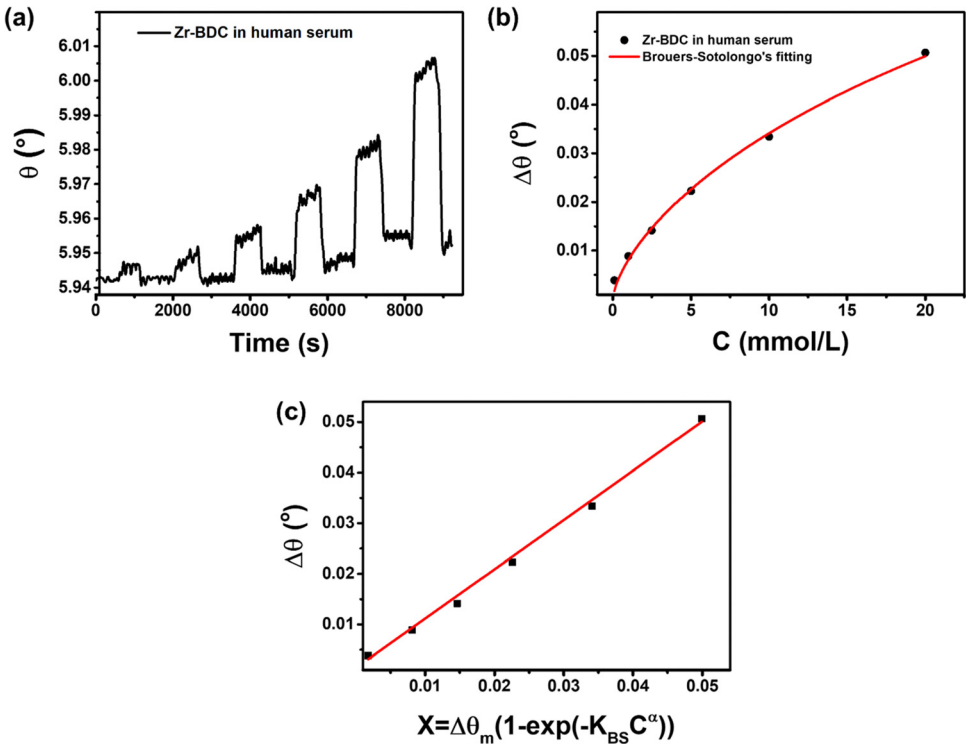

Fig. 8 (a) SPR dynamic response, (b) the Brouers–Sotolongo isotherm adsorption model fitting, and (c) the calibration curve of the hierarchical plate-like Zr-BDC to 0.1–20 mmol L^{-1} glucose in a human serum/PBS solution.

Table 3 The LOD comparison of the Zr-BDC-functionalized SPR sensor with other SPR sensors for glucose detection

SPR type	Recognition layer	Detection step	Medium solution	Concentration range	LOD (S/N = 3)	Ref.
Fiber optic	SiO_2/GO_x	Separated	PBS	0–80 mg dL^{-1} (0–4.44 mmol L^{-1})	0.142 mg mL^{-1} (0.788 mmol L^{-1})	83
Fiber optic	AuNps/P-mercaptophenyl-boronic acid (PMBA)	Separated	PBS	0–1.7 mmol L^{-1}	0.00078 mmol L^{-1}	84
Fiber optic	Ag/Au film/4-mercaptophenyl-boronic acid (4-MPBA)	Separated	PBS	0–0.1 mmol L^{-1}	0.00112 mmol L^{-1}	85
Prism coupler	Cr-Au/Ta_2O_5	Separated	DI water and 2% lipofundin	0–500 mg dL^{-1} (0–27.75 mmol L^{-1})	3.72 mg dL^{-1} (0.21 mmol L^{-1})	87
Prism coupler	Glucose oxidase@silica mesocellular foams/SiO_2 nanoparticles (GO_x@SiMCFs/SiNPs)	Separated	PBS	0–200 mg dL^{-1} (0–11.21 mmol L^{-1})	2.22 mmol L^{-1}	14
Prism coupler	Au/Zr-BDC film	Continued	Human serum – PBS	0.1–20 mmol L^{-1}	0.482 mmol L^{-1}	This work

detection performance of the Zr-BDC-functionalized SPR sensor in a mixture of PBS and commercial human serum with a volume ratio of 100 : 1. The dynamic response of the Zr-BDC-functionalized SPR sensor toward different concentrations of glucose (0.1–20 mmol L^{-1}) is shown in Fig. 8a with changes in the response values summarized in Table S6 (ESI†). Isotherm analysis of the *C vs.* $\Delta\theta$ curve shows good agreement with the Brouers–Sotolongo model with R^2 = 0.99576 (Fig. 8b). This suggests that the mechanism of glucose detection in human serum follows the same model as in PBS only. However, there are differences in the parameters obtained, such as $\Delta\theta_m$, α, and K_{BS}, with values of 0.1267 mmol g^{-1}, 0.066, and 0.676, respectively. Furthermore, the exponent α value is less than 1, indicating that the initial adsorption kinetics process occurs quickly so that the active site on the hierarchical Zr-BDC MOF can enable the adsorption of many glucose molecules.[57] A slight reduction in the $\Delta\theta_m$ value is also observed for SPR measurement in a human serum/PBS mixture compared to that in PBS only because the initial concentration adsorbed can affect the adsorption capacity.[82]

The glucose detection performance of the Zr-BDC-functionalized SPR sensor in a human serum/PBS mixture is better than that in PBS alone. The calibration curve in Fig. 8c produces a linear equation $\Delta\theta = 0.97396X + 0.00142$ with an R^2 value of 0.99806. The slope of the line is not much different than that obtained in PBS solution, but the LOD is much lower in human serum/PBS mixture (0.482 mmol L^{-1} (S/N = 3)), indicating the enhanced sensing performance. This improvement is attributed to the presence of human serum in solution, which can increase the mass of the captured molecules, hence increasing its stability and refractive index. Next, from the dynamic response-recovery curves, the sensitivities obtained from calibration measurements in the human serum/PBS mixture and pure PBS are 0.97702 and 0.97396, respectively, were compared. The high sensitivity of the Zr-BDC-functionalized SPR sensor can be developed further and used in practical applications.

As shown in Table 3, although some previous SPR sensors exhibit a lower LOD than our Zr-BDC-functionalized SPR sensor, and they require the use of GO_x or phenyl boronic acid (PBA) as a glucose receptor. Meanwhile, other SPR sensors only work within a small concentration range of glucose (0–5 mmol L^{-1}), whereas the glucose concentration in the blood of diabetics is usually more than 11.1 mmol L^{-1} under normal conditions and higher than 7 mmol L^{-1} in a fasting state.[83–86] With a LOD of 0.482 mmol L^{-1}, the developed Zr-BDC-functionalized SPR sensor can detect glucose concentrations in people with diabetes (0 to 20 mmol L^{-1}). Furthermore, the LOD value of our SPR sensor is below that required by the Food and Drug Administration (FDA, United States) for point-of-care diabetes detection tool, which is 10 mg dL^{-1} or 0.555 mmol L^{-1}.[87] Therefore, the Zr-BDC-functionalized SPR sensor has the potential to be used in a POC device and compete with other detection devices that use other natural glucose receptors.

4. Conclusions

This study has demonstrated that the modification of a standard SPR sensor chip with hierarchical M-BDC MOFs to enhance the sensing response towards small molecules, such as glucose. The adsorption mechanism of glucose by M-BDC MOFs varies depending on the metal center. The adsorption isotherms of Cu-BDC, Mn-BDC, and Ni-BDC follow the Langmuir–Freundlich adsorption model. In contrast, the adsorption of glucose on Zr-BDC follows the Brouers–Sotolongo adsorption model. Among the M-BDC MOFs, the glucose adsorption is fastest in Zr-BDC as it occurs by diffusion with K_{AV} = 0.66681 s^{-1}. The FTIR spectra of the M-BDC MOFs after glucose adsorption show the strengthening of the C–O and O–H stretching vibrations, except for Mn-BDC. Therefore, the binding of glucose to M-BDC MOFs occurs through interactions with the O–H and C–O groups. The calibration curves obtained from the dynamic response data of M-BDC MOFs reveal that Zr-BDC exhibits a higher slope value (*i.e.*, higher sensitivity) than other M-BDC MOFs. Furthermore, it has a better LOD for glucose sensing in concentration range of 0.1–20 mmol L^{-1}

than Cu-BDC, Ni-BDC, Mn-BDC and bare Au substrate in the concentration range of 5–20 mmol L^{-1}. The Zr-BDC-functionalized SPR sensor also displays good selectivity towards glucose in the presence of other interfering compounds, such as ascorbic acid, uric acid, urea, and maltose. In addition, it shows a stronger binding towards glucose than fructose and sucrose. The reusability test of the Zr-BDC-functionalized SPR sensor shows that its dynamic response decreases from 100% to 91.5%, 52.72%, 49.46%, and 37.04% after the 2nd, 3rd, 4th, and 5th measurement, respectively. In the future, the reusability aspect of this sensor will be improved further by hybridization with other materials. The glucose sensing test in a human serum/PBS mixture shows an increase in the glucose sensing performance of the Zr-BDC-functionalized SPR sensor than in PBS alone with a ten times smaller LOD. In our future work, this sensor will be further improved to enable its application in point-of-care devices for diabetes detection.

Conflicts of interest

There are no conflicts to declare.

Acknowledgements

The authors acknowledge financial grants provided by Lembaga Pengelola Dana Pendidikan (LPDP), Ministry of Finance of Indonesia. This work is also partially supported by Indonesia Ministry of Education, Culture, Research, and Technology, and the research grant of Institut Teknologi Bandung (ITB). J. H. acknowledges the funding from Japan Society for the Promotion of Science (JSPS) KAKENHI Program (Grant no. 20K05453). Y. V. K. acknowledges the funding from Advance Queensland (AQIRF043-2020-CV).

References

1 World Health Organization, *Global report on diabetes*, World Health Organization, Geneva, 2016.
2 V. Scognamiglio, *Biosens. Bioelectron.*, 2013, **47**, 12–25.
3 H.-C. Wang and A.-R. Lee, *J. Food Drug Anal.*, 2015, **23**, 191–200.
4 International Diabetes Federation, *IDF Diabetes Atlas* Ninth Edition, 2019.
5 E. Wijaya, C. Lenaerts, S. Maricot, J. Hastanin, S. Habraken, J.-P. Vilcot, R. Boukherroub and S. Szunerits, *Curr. Opin. Solid State Mater. Sci.*, 2011, **15**, 208–224.
6 X. Guo, *J. Biophoton.*, 2012, **5**, 483–501.
7 J. Homola, S. S. Yee and G. Gauglitz, *Sens. Actuators, B*, 1999, **54**, 3–15.
8 W. W. Lam, L. H. Chu, C. L. Wong and Y. T. Zhang, *Sens. Actuators, B*, 2005, **105**, 138–143.
9 N. K. Singh, B. Jain and S. Annapoorni, *Sens. Actuators, B*, 2011, **156**, 383–387.
10 J. Li, D.-f Lu, Z. Zhang, Q. Liu and Z.-m Qi, *Sens. Actuators, B*, 2014, **203**, 690–696.
11 H. V. Hsieh, Z. A. Pfeiffer, T. J. Amiss, D. B. Sherman and J. B. Pitner, *Biosens. Bioelectron.*, 2004, **19**, 653–660.
12 W. Wu, J. Shen, Y. Li, H. Zhu, P. Banerjee and S. Zhou, *Biomaterials*, 2012, **33**, 7115–7125.
13 L. Kumar, R. Gupta, D. Thakar, V. Vibhu and S. Annapoorni, *Plasmonics*, 2013, **8**, 487–494.
14 Y. Yuan, N. Yuan, D. Gong and M. Yang, *Photon. Sens.*, 2019, **9**, 309–316.
15 M.-S. Steiner, A. Duerkop and O. S. Wolfbeis, *Chem. Soc. Rev.*, 2011, **40**, 4805–4839.
16 M. Lobry, D. Lahem, M. Loyez, M. Debliquy, K. Chah, M. David and C. Caucheteur, *Biosens. Bioelectron.*, 2019, **142**, 111506.
17 A. Stephenson-Brown, H.-C. Wang, P. Iqbal, J. A. Preece, Y. Long, J. S. Fossey, T. D. James and P. M. Mendes, *Analyst*, 2013, **138**, 7140–7145.
18 X. Sun and T. D. James, *Chem. Rev.*, 2015, **115**, 8001–8037.
19 N. Pal, B. Saha, S. K. Kundu, A. Bhaumik and S. Banerjee, *New J. Chem.*, 2015, **39**, 8035–8043.
20 N. Pal, S. Banerjee and A. Bhaumik, *J. Colloid Interface Sci.*, 2018, **516**, 121–127.
21 P. J. Lynch, A. Amorim Graf, S. P. Ogilvie, M. J. Large, J. P. Salvage and A. B. Dalton, *J. Mater. Chem. B*, 2020, **8**, 7733–7739.
22 X. Xuan, M. Qian, L. Pan, T. Lu, L. Han, H. Yu, L. Wan, Y. Niu and S. Gong, *J. Mater. Chem. B*, 2020, **8**, 9094–9109.
23 H. Zou, D. Tian, C. Lv, S. Wu, G. Lu, Y. Guo, Y. Liu, Y. Yu and K. Ding, *J. Mater. Chem. B*, 2020, **8**, 1008–1016.
24 D. Chu, Y. Wang, D. Li, X.-Q. Chu, D. Ge and X. Chen, *Dalton Trans.*, 2022, **51**, 15354–15360.
25 X. Zha, W. Yang, L. Shi, Q. Zeng, J. Xu and Y. Yang, *Dalton Trans.*, 2023, **52**, 2631–2640.
26 W. Liu and X.-B. Yin, *TrAC, Trends Anal. Chem.*, 2016, **75**, 86–96.
27 C.-H. Chuang and C.-W. Kung, *Electroanalysis*, 2020, **32**, 1885–1895.
28 Y. Xu, Q. Li, H. Xue and H. Pang, *Coord. Chem. Rev.*, 2018, **376**, 292–318.
29 H. Li, L. Shi, C. Li, X. Fu, Q. Huang and B. Zhang, *ACS Appl. Mater. Interfaces*, 2020, **12**, 34095–34104.
30 L. Hang, F. Zhou, D. Men, H. Li, X. Li, H. Zhang, G. Liu, W. Cai, C. Li and Y. Li, *Nano Res.*, 2017, **10**, 2257–2270.
31 G. Zhu, M. Zhang, L. Lu, X. Lou, M. Dong and L. Zhu, *Sens. Actuators, B*, 2019, **288**, 12–19.
32 G. Gumilar, Y. V. Kaneti, J. Henzie, S. Chatterjee, J. Na, B. Yuliarto, N. Nugraha, A. Patah, A. Bhaumik and Y. Yamauchi, *Chem. Sci.*, 2020, **11**, 3644–3655.
33 Z. Zeng, J. Lyu, P. Bai and X. Guo, *Ind. Eng. Chem. Res.*, 2018, **57**, 9200–9209.
34 A. Göçenoğlu Sarıkaya, B. Osman, T. Çam and A. Denizli, *Sens. Actuators, B*, 2017, **251**, 763–772.
35 A. M. M. Vargas, A. L. Cazetta, M. H. Kunita, T. L. Silva and V. C. Almeida, *Chem. Eng. J.*, 2011, **168**, 722–730.
36 M. A. Ahmad, N. Ahmad and O. S. Bello, *Appl. Water Sci.*, 2015, **5**, 407–423.
37 M. A. H. D. Allah, S. N. Taqui, U. T. Syed and A. A. Syed, *SN Appl. Sci.*, 2019, **1**, 330.

38 M. Brdar, M. Šćiban, A. Takači and T. Došenović, *Chem. Eng. J.*, 2012, **183**, 108–111.
39 N. Ayawei, A. N. Ebelegi and D. Wankasi, *J. Chem.*, 2017, **2017**, 3039817.
40 R. Seetharaj, P. V. Vandana, P. Arya and S. Mathew, *Arabian J. Chem.*, 2019, **12**, 295–315.
41 U. S. Kestur, H. Lee, D. Santiago, C. Rinaldi, Y.-Y. Won and L. S. Taylor, *Cryst. Growth Des.*, 2010, **10**, 3585–3595.
42 J. Henzie, V. Etacheri, M. Jahan, H. Rong, C. N. Hong and V. G. Pol, *J. Mater. Chem. A*, 2017, **5**, 6079–6089.
43 Y. Borodko, S. M. Humphrey, T. D. Tilley, H. Frei and G. A. Somorjai, *J. Phys. Chem. C*, 2007, **111**, 6288–6295.
44 S. Chowdhury, N. L. Torad, A. Ashok, G. Gumilar, W. Chaikittisilp, R. Xin, P. Cheng, M. I. Ul Hoque, M. A. Wahab, M. R. Karim, B. Yuliarto, M. S. Hossain, Y. Yamauchi and Y. V. Kaneti, *Chem. Eng. J.*, 2022, **450**, 138065.
45 W. Qian, Y. Tan, Y. Yu, L. Zhang, X. Wu and B. Xue, *J. Alloys Compd.*, 2022, **918**, 165741.
46 M. Shete, P. Kumar, J. E. Bachman, X. Ma, Z. P. Smith, W. Xu, K. A. Mkhoyan, J. R. Long and M. Tsapatsis, *J. Membrane Sci.*, 2018, **549**, 312–320.
47 N. L. Rosi, J. Kim, M. Eddaoudi, B. Chen, M. O'Keeffe and O. M. Yaghi, *J. Am. Chem. Soc.*, 2005, **127**, 1504–1518.
48 A. Carton, A. Mesbah, T. Mazet, F. Porcher and M. François, *Solid State Sci.*, 2007, **9**, 465–471.
49 J. H. Cavka, S. Jakobsen, U. Olsbye, N. Guillou, C. Lamberti, S. Bordiga and K. P. Lillerud, *J. Am. Chem. Soc.*, 2008, **130**, 13850–13851.
50 S. Gao, Y. Sui, F. Wei, J. Qi, Q. Meng and Y. He, *J. Mater. Sci.*, 2018, **53**, 6807–6818.
51 S. Yuan, L. Feng, K. Wang, J. Pang, M. Bosch, C. Lollar, Y. Sun, J. Qin, X. Yang, P. Zhang, Q. Wang, L. Zou, Y. Zhang, L. Zhang, Y. Fang, J. Li and H.-C. Zhou, *Adv. Mater.*, 2018, **30**, 1704303.
52 K. Tan, N. Nijem, P. Canepa, Q. Gong, J. Li, T. Thonhauser and Y. J. Chabal, *Chem. Mater.*, 2012, **24**, 3153–3167.
53 K. Tan, N. Nijem, Y. Gao, S. Zuluaga, J. Li, T. Thonhauser and Y. J. Chabal, *CrystEngComm*, 2015, **17**, 247–260.
54 Ü. Kökçam-Demir, A. Goldman, L. Esrafili, M. Gharib, A. Morsali, O. Weingart and C. Janiak, *Chem. Soc. Rev.*, 2020, **49**, 2751–2798.
55 Y. Keren, M. Borisover and N. Bukhanovsky, *Chemosphere*, 2015, **138**, 462–468.
56 M. A. Al-Ghouti and D. A. Da'ana, *J. Hazard. Mater.*, 2020, **393**, 122383.
57 S. Karoui, R. Ben Arfi, K. Mougin, A. Ghorbal, A. A. Assadi and A. Amrane, *J. Hazard. Mater.*, 2020, **387**, 121675.
58 F. Brouers and T. J. Al-Musawi, *J. Mol. Liq.*, 2015, **212**, 46–51.
59 F. Brouers, *J. Modern Phys.*, 2014, **5**, 1594–1601.
60 R. Abazari, A. R. Mahjoub and J. Shariati, *J. Hazard. Mater.*, 2019, **366**, 439–451.
61 N. A. Oladoja, *Desalination Water Treat.*, 2016, **57**, 15813–15825.
62 J. C. Soares, A. C. Soares, P. A. R. Pereira, V. D. C. Rodrigues, F. M. Shimizu, M. E. Melendez, C. Scapulatempo Neto, A. L. Carvalho, F. L. Leite, S. A. S. Machado and O. N. Oliveira, *Phys. Chem. Chem. Phys.*, 2016, **18**, 8412–8418.
63 N. K. Gupta, A. Sengupta, V. G. Rane and R. M. Kadam, *Sep. Sci. Technol.*, 2017, **52**, 2049–2061.
64 C. Nanthamathee and P. Dechatiwongse, *Mater. Chem. Phys.*, 2021, **258**, 123924.
65 C. E. Housecroft and A. G. Sharpe, *Inorganic chemistry*, Pearson Prentice Hall, Harlow, England, 2nd edn, 2005.
66 M. Zhang, K. Gu, X. Huang and Y. Chen, *Phys. Chem. Chem. Phys.*, 2019, **21**, 19226–19233.
67 H.-A. Tajmir-Riahi, *Carbohyd. Res.*, 1988, **183**, 35–46.
68 S. Zuluaga, E. M. A. Fuentes-Fernandez, K. Tan, F. Xu, J. Li, Y. J. Chabal and T. Thonhauser, *J. Mater. Chem. A*, 2016, **4**, 5176–5183.
69 D. Lv, J. Chen, Y. Chen, Z. Liu, Y. Xu, C. Duan, H. Wu, Y. Wu, J. Xiao, H. Xi, Z. Li and Q. Xia, *AIChE J.*, 2019, **65**, e16616.
70 J. J. Low, A. I. Benin, P. Jakubczak, J. F. Abrahamian, S. A. Faheem and R. R. Willis, *J. Am. Chem. Soc.*, 2009, **131**, 15834–15842.
71 J. Canivet, A. Fateeva, Y. Guo, B. Coasne and D. Farrusseng, *Chem. Soc. Rev.*, 2014, **43**, 5594–5617.
72 T. Sathvika, S. Balaji, M. Chandra, A. Soni, V. Rajesh and N. Rajesh, *Chem. Eng. J.*, 2019, **360**, 879–889.
73 J. B. DeCoste, G. W. Peterson, H. Jasuja, T. G. Glover, Y.-G. Huang and K. S. Walton, *J. Mater. Chem. A*, 2013, **1**, 5642–5650.
74 Y. Wu, X. Song, S. Li, J. Zhang, X. Yang, P. Shen, L. Gao, R. Wei, J. Zhang and G. Xiao, *J. Ind. Eng. Chem.*, 2018, **58**, 296–303.
75 W. Zheng, W. Bi, X. Gao, Z. Zhang, W. Yuan and L. Li, *Sustain. Energy Fuels*, 2020, **4**, 5757–5764.
76 L. G. Beka, X. Bu, X. Li, X. Wang, C. Han and W. Liu, *RSC Adv.*, 2019, **9**, 36123–36135.
77 Y. Huang, C.-A. Tao, R. Chen, L. Sheng and J. Wang, *Nanomaterials*, 2018, **8**, 676.
78 E. Redel, Z. Wang, S. Walheim, J. Liu, H. Gliemann and C. Wöll, *Appl. Phys. Lett.*, 2013, **103**, 091903.
79 R. Dorey, in *Ceramic Thick Films for MEMS and Microdevices*, ed. R. Dorey, William Andrew Publishing, Oxford, 2012, pp. 85–112, DOI: 10.1016/B978-1-4377-7817-5.00004-3.
80 G. Gumilar, J. Henzie, B. Yuliarto, A. Patah, N. Nugraha, M. Iqbal, M. A. Amin, M. S. A. Hossain, Y. Yamauchi and Y. V. Kaneti, *J. Mater. Chem. A*, 2022, **10**, 6662–6678.
81 A. Ali, Y. W. Chiang and R. M. Santos, *Journal*, 2022, **12**, 205.
82 N. H. Othman, N. H. Alias, M. Z. Shahruddin, N. F. Abu Bakar, N. R. Nik Him and W. J. Lau, *J. Environ. Chem. Eng.*, 2018, **6**, 2803–2811.
83 Y. Yuan, X. Yang, D. Gong, F. Liu, W. Hu, W. Cai, J. Huang and M. Yang, *Opt. Express*, 2017, **25**, 3884–3898.
84 W.-L. Zheng, Y.-N. Zhang, L.-K. Li, X.-G. Li and Y. Zhao, *Biosens. Bioelectron.*, 2022, **198**, 113798.
85 X. Wang, X. Sun, Y. Hu, L. Zhang, L. Zeng, Q. Liu and J. Duan, *IEEE Sens. J.*, 2022, **22**, 20413–20420.
86 B. L. Furman, *Reference Module in Biomedical Sciences*, Elsevier, 2017, DOI: 10.1016/B978-0-12-801238-3.98060-7.
87 Q.-H. Phan, Y.-R. Lai, W.-Z. Xiao, T.-T.-H. Pham and C.-H. Lien, *Opt. Express*, 2020, **28**, 24889–24899.

